



# Evaluating Size Effects for a Porous, Weak, Homogeneous Limestone

Sankhaneel Sinha<sup>1,2</sup> · Gabriel Walton<sup>1</sup> · Akash Chaurasia<sup>1</sup> · Mark Diederichs<sup>3</sup> · Timothy Batchler<sup>4</sup>

Received: 23 February 2022 / Accepted: 3 November 2022 / Published online: 22 November 2022  
© The Author(s), under exclusive licence to Springer-Verlag GmbH Austria, part of Springer Nature 2022

## Abstract

In rock engineering, size effects have been a topic of extensive research since the early 1960s, and despite many advances over the years, our understanding of size effect remains incomplete, especially for weak, porous, homogeneous rocks. Indeed, the vast majority of studies related to size effect have specifically considered low porosity rocks (generally crystalline). To bridge this gap in knowledge, we conducted unconfined compression tests on cubic limestone blocks ranging in size from 0.1 to 0.9 m. Texas Cream Limestone, which is a porous, homogeneous, weak rock, was chosen for this study. As this rock has not previously been studied in the literature, conventional compression tests and indirect tensile strength tests on cylindrical specimens were completed prior to testing the cube specimens. For the largest specimens, 3D digital image correlation (3D-DIC) was employed to track the surficial displacements as a function of the applied load. The tests revealed a lack of size effect for the entire range of block sizes considered. To evaluate size effects more broadly, data from prior studies on sedimentary rocks were compiled, and a tendency for the magnitude of the size effect on strength to decline with increasing porosity was noted. Some hypotheses regarding this trend are presented and evaluated based on strain-field heterogeneity metrics obtained from the 3D-DIC analysis.

## Highlights

- Unconfined compression tests were conducted on limestone blocks ranging in size from 0.1 m to 0.9 m side length.
- Negligible size effect on strength was observed in this weak, porous, homogeneous limestone.
- 3D-Digital Image Correlation analysis was performed to obtain strain fields as a function of applied load for the two largest specimens.
- Contrary to low-porosity rocks, more heterogeneity in strain field was noted in the axial direction in comparison to the lateral direction
- A compilation of data from the literature indicates that increased porosity may dampen size effects.

**Keywords** Size effect · Porous limestone · Soft rock · Digital image correlation · Strain heterogeneity

## 1 Introduction

Size effect refers to the change in mechanical characteristics of a rock as a function of specimen size. Since most engineering designs require material properties at a scale much larger than those conventionally measured in laboratory, development of ‘upscaling’ techniques has been a topic of extensive research over the past few decades. The empirical approach is most common, where models for size effects are established by fitting curves to properties (e.g., strength) obtained from laboratory and/or field tests. The

---

✉ Sankhaneel Sinha  
sankhaneelsinha@mines.edu

<sup>1</sup> Colorado School of Mines, Golden, CO, USA

<sup>2</sup> Golder Associates (WSP), Phoenix, AZ, USA

<sup>3</sup> Geological Engineering, Queen’s University, Kingston, ON, Canada

<sup>4</sup> National Institute for Occupational Safety and Health, Pittsburgh, USA

most well-known work in this regard is that by Hoek and Brown (1980).

Numerous other studies have been conducted over the years to improve our understanding of size effect in rocks (e.g., Mogi 1961; Hoskins and Horino 1969; Nishimatsu et al. 1969; Pratt et al. 1972; Brace 1981; Jackson and Lau 1990; Cunha 1990; Martin 1997; Hawkins 1998; Thuro et al. 2001; Pells 2004; Yoshinaka et al. 2008; Darlington et al. 2011; Masoumi et al. 2016; Quiñones et al. 2017; Jaczkowski et al. 2017; Walton 2018). In most of these studies, a moderate to significant decline in strength has been reported with an increase in specimen size for all three rock types—igneous, sedimentary, and metamorphic. Some studies like Pells (2004) have indicated a lack of size effect in weak, porous, homogeneous rocks like Hawkesbury Sandstone. Pells (2004) explained the lack of size effect by stating that the Hawkesbury Sandstone specimens did not have pre-existing flaws (i.e., microcracks), as they were akin to pure quartz sand. On the contrary, Hawkins (1998) and more recently Zhai et al. (2020) have demonstrated a modest size effect on strength for some homogeneous weak rocks. While one could systematically compare data from literature to resolve this ambiguity, the vast majority of prior size effect studies have considered strong, low porosity rocks, and little data is available on weak, porous intact rocks to conduct such a comparison (Yoshinaka et al. 2008).

Size effects in intact rocks are often explained in context of the influence of the number of grains included in a specimen (Hoek and Brown 1980). For example, larger specimens will contain more grain-scale flaws (Sprunt and Brace 1974; Tapponier and Brace 1976; Kranz 1983), which may act as weak links in the brittle microfracturing process, ultimately leading to a reduced strength for a larger specimen volume (Weibull 1939; Diederichs 2003; Masoumi 2013). Numerous authors in the past have advocated for this explanation of size effect (e.g., Mogi 1961; Bandis 1980; Jackson and Lau 1990; Yoshinaka et al. 2008; Quiñones et al. 2017). Since flaws concentrate stresses, one might expect the size effect to vanish completely at large confining stress. Indeed, limited data in literature supports this statement (Bernaix 1974; Baecher and Einstein 1981; Barton 1990; Walton 2018), which in turn is consistent with the weak-link explanation.

Cunha (1990) suggested that size effect in intact rocks is basically due to heterogeneity, and heterogeneity increases when: (1) the number of mineral components increases, (2) variation of characteristics among the constituent minerals increases, (3) differences in the sizes of the components increase, (4) there is a similar percentage of all components; if percentage of one component increases toward 100%, then heterogeneity tends to homogeneity, (5) spatial non-uniformity of the distribution of

mineral components increases, i.e., instead of a random distribution of all the mineral components in the volume, there are concentrations of certain component in different regions. Cunha (1990)'s description, therefore, considers both elastic and geometric heterogeneity (Lan et al. 2010).

Cunha (1990)'s conceptual model explains why igneous rocks like granite (grains with different shapes, sizes, and mechanical properties; Bass 1995) exhibit significant size effects; the elastic mismatch or heterogeneity between the different mineral grains promotes the development of grain-scale flaws either during its depositional history and/or during specimen extraction (Dey and Wang 1981; Kranz 1983). For rocks composed primarily of a single mineral (e.g., limestone and sandstone) size effects should therefore be limited or absent. While this is consistent with data presented by Hoskins and Horino (1969), Pells (2004), Masoumi et al. (2016), and Li et al. (2021), it is at odds with the findings of Hawkins (1998) and Zhai et al. (2020) (see Fig. 1).

To further investigate size effects in homogeneous rocks and contribute to the database of results published in the literature, we conducted unconfined compression tests on a porous limestone (Texas Cream Limestone) using blocks ranging in edge length from 0.1 to 0.9 m. 3D digital image correlation (3D-DIC) was employed to monitor the full-field displacements for the largest specimens. Conventional uniaxial compressive strength (UCS) tests and Brazilian tensile strength (BTS) tests were also conducted

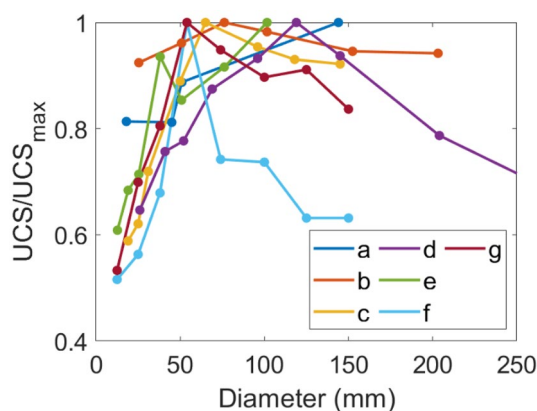


**Fig. 1** Normalized UCS as a function of specimen diameter from six prior studies. The rock names, maximum UCS, and citations are as follows: **a** 31.1 MPa—Hawkesbury Sandstone (Pells 2004); **b** 52.3 MPa—Kansas Limestone (Hoskin and Horino 1969); **c** 58.8 MPa—Gosford Sandstone (Masoumi et al. 2016); **d** 4.0 MPa—Gambier Limestone (Zhai et al. 2020) **e** 46.5 MPa—Berea Sandstone (Li et al. 2021); **f** 19 MPa—Bathstone (Hawkins 1998); **g** 34.9 MPa—Hollington Sandstone (Hawkins 1998). Rocks with low UCS were chosen preferentially as it is most relevant to the current study

prior to testing the cube-shaped specimens to geomechanically characterize the rock.

## 2 Description and Geomechanical Characterization of Texas Cream Limestone

Texas Cream Limestone is a lower Cretaceous (100.5–145 Ma) fossilized, light beige-cream white carbonate rock and can be classified as a grainstone, based on Dunham's classification (Dunham 1962). It is generally used for wall and floor tiles, countertops, stairs, window sills, etc. A theoretical calculation considering a carbonate grain density of 2708 kg/m<sup>3</sup> (Sitepu 2009) and average bulk density of 2003 kg/m<sup>3</sup> returns a porosity value of 26% for Texas Cream Limestone. This value is consistent with those reported by Liaw et al. (1996) and Weber et al. (2021).

To geomechanically characterize this rock, conventional UCS and BTS tests were conducted on nine and seven specimens, respectively, at the Earth Mechanics Institute laboratory at the Colorado School of Mines. Tests were conducted using an MTS compression loading frame following relevant ASTM-suggested methods (ASTM D7012-04 2004; ASTM 3967-16 2016). The tests were conducted in a load-controlled mode with a rate of 150 N/s. Geometrical details of the UCS specimens are presented in Table 1, and some representative test specimens are shown in Fig. 2. The axial and lateral displacements for the UCS specimens were monitored using two separate extensometers (Fig. 3a). Table 1 summarizes the UCS test results for the nine specimens; the mean UCS, Young's modulus, and Poisson's ratio are 13.9 MPa, 10.9 GPa, and 0.15, respectively. The indirect tensile strength, per the BTS tests, is  $1.7 \pm 0.2$  MPa (mean + 1 standard deviation). Perras and Diederichs (2014) proposed a correction factor of 0.68 for converting indirect tensile strength to direct



**Fig. 2** UCS (left) and BTS (right) specimens of Texas Cream Limestone

tensile strength for sedimentary rocks. Using this value, a UCS to tensile strength ( $\sigma_t$ ) ratio of 12.1 was obtained for Texas Cream Limestone.  $UCS/\sigma_t$  is a well-recognized material brittleness index and is approximately equivalent to the Hoek Brown  $m_i$  parameter (valid when  $UCS/\sigma_t > 8$ ; Cai 2010).

The axial and lateral stress–strain curves for the nine UCS tests and a representative post-testing fracture pattern for one specimen are shown in Figs. 4 and 3b, respectively. Splitting fractures were observed in most of the specimens with limited shearing (see Fig. 3b for an example). The moderate  $UCS/\sigma_t$  value and the fracture pattern imply that Texas Cream Limestone could exhibit ductile behavior over a relatively small range of confining pressure (Walton et al. 2015; Walton 2021), but under unconfined/low confinement conditions, damage still primarily occurs in extension (macroscopic axial cracking or coalescence of small, axially oriented cracks) as is typically the case for

**Table 1** UCS, Young's modulus, and Poisson's ratio for nine standard cylindrical specimens of Texas Cream Limestone

Specimen name	Specimen diameter (mm)	Length to diameter ratio	UCS (MPa)	Young's modulus or E (GPa)	Poisson's ratio or $\nu$
LST-1	51.18	2.51	13.5	10.2	0.14
LST-2	51.13	2.44	15.1	10.4	0.18
LST-3	51.16	2.25	13.7	10.1	0.13
LST-4	51.21	2.42	14.6	9.1	0.14
LST-5	51.18	2.44	14.7	10.8	0.14
LST-6	51.13	2.43	14.4	9.0	0.13
LST-7	51.13	2.42	13.6	12.1	0.20
LST-8	51.21	2.45	11.1	15.4	0.17
LST-10	51.23	2.42	14.0	11.0	0.10
Mean	51.17	2.42	13.9	10.9	0.15

**Fig. 3** **a** Setup for the UCS test, **b** fracture pattern for LST-3 specimen

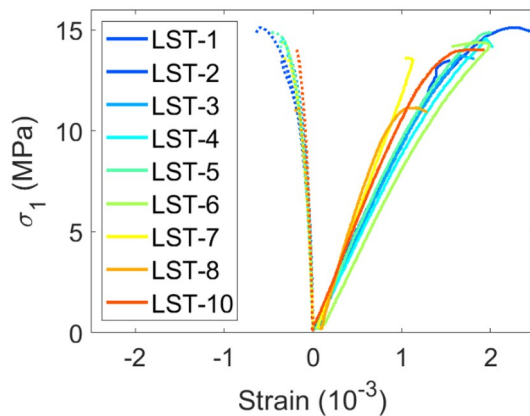
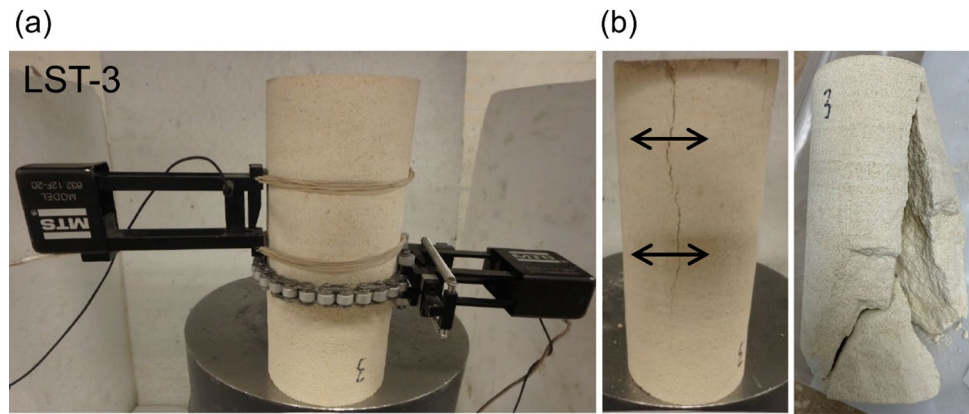


**Fig. 4** Stress–strain curves for the nine UCS tests. Post-peak behaviors could not be obtained as the tests were run in load-controlled mode

all but the most ductile rocks (Wong and Baud 2012; Walton 2021).

### 3 Test Setup for Size Effect Study

#### 3.1 Specimen Description

To study the size effect on Texas Cream Limestone strength, 14 unconfined compression tests were conducted on cubic specimens with five different edge lengths—0.1 m ( $0.095 \pm 0.005$  m; 5 specimens), 0.2 m ( $0.196 \pm 0.002$  m; 5 specimens), 0.3 m ( $0.297 \pm 0.002$  m; 2 specimens), 0.7 m ( $0.697 \pm 0.001$  m; 1 specimen), and 0.9 m ( $0.898 \pm 0.001$  m; 1 specimen). The exact edge lengths of each specimen are reported in Appendix A. For naming purposes, the specimen groups for each size are identified based on their edge length rounded to the nearest 0.1 m, although all analyses presented in this paper are based on the actual dimensions of the specimens.

The 0.2–0.9 m specimens were bought pre-cut from a quarry in New Mexico. One of the 0.2 m blocks was further divided into multiple 0.1 m specimens at Colorado School of Mines and then ground to ASTM specifications (ASTM 4543-85, 2001). Based on the size of the grinding machine used, it was not possible to smooth the loading faces of the 0.2–0.9 m blocks. The parallelism of the loading faces was measured by placing the specimens on a level surface and measuring the heights at various points along the four vertical faces; these measurements are reported in Appendix A. Only those specimens that exhibited adequate parallelism were ultimately used for the compression tests (see Appendix A for more details).

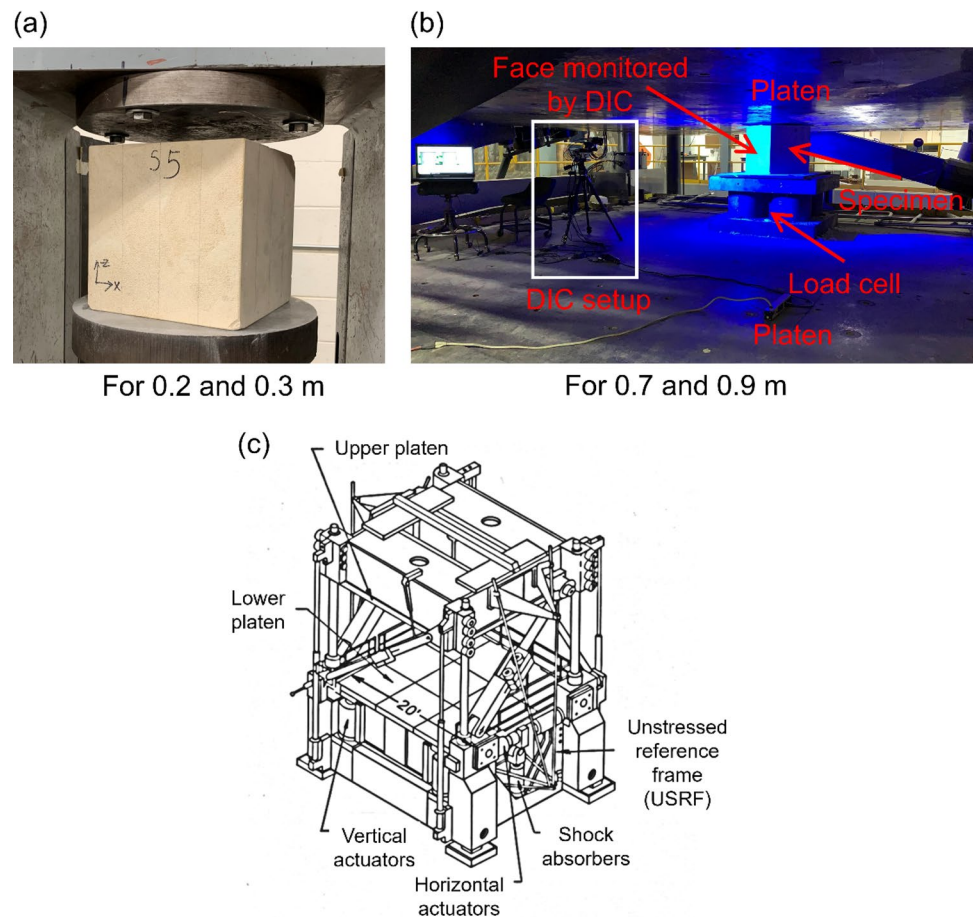
#### 3.2 Testing Procedure Information

The compression tests on 0.1–0.3 m blocks were conducted using two different MTS machines at Colorado School of Mines, while the compression tests on the larger blocks were completed at the NIOSH facility in Pittsburgh using the mine roof simulator (MRS; Fig. 5). A schematic of the MRS can be found in Fig. 5c (Barczak 2000), and more details are presented later.

There are two reasons for using two different MTS machines for the 0.1–0.3 m tests: (1) the largest capacity machine could load all three sizes to peak strength, but its displacement range was insufficient to bring the platens in contact with the 0.1 m specimens; (2) the lower capacity machine did not have large enough platens to load the 0.2 m and 0.3 blocks. Ultimately, the 0.1 m blocks were tested in the same machine as the UCS tests were conducted (discussed under Sect. 2; load control mode), while the 0.2 and 0.3 m block tests were performed in the higher capacity MTS machine in displacement control mode (Fig. 5). In this case, by setting a constant axial displacement rate of 5  $\mu\text{m/s}$ , it was possible to obtain the post-peak response for both the 0.2 m and 0.3 m specimens. Extensometers could not be used to measure specimen deformation because of the square profile of the specimens (the rubber band could



**Fig. 5** Experimental setup for the **a** 0.2 m and 0.3 m block test, and **b** 0.7 and 0.9 m block test. The 0.7 m and 0.9 m blocks were placed on a load cell, and one of their vertical faces was monitored using 3D-DIC. **c** Schematic of MRS (from Barczak 2000)



not be made taut; see Fig. 3a), and only the load and platen displacements from the MTS machine were available for analysis. This means that the displacement measurements from the MTS included a system deformation component (i.e., strains associated with the different platen arrangements for specimens of different sizes) and are not direct measurements representative of specimen strain.

The MRS is a servo-controlled hydraulic press custom built by MTS for the US Bureau of Mines in 1979. It was originally designed for testing longwall shields and is currently the only load frame in the USA that can accommodate full-size shield supports (Barczak 2005). The MRS has several distinctive characteristics. It has a 6 m × 6 m platen made of steel, and the upper platen can be moved vertically on directional columns and clamped at any specific position. The maximum separation allowed between the upper and lower platen is 4.87 m. Load is applied by controlling the movement of the lower platen, either in load or displacement control mode. The MRS has a load capacity of 14.715 MN and a maximum vertical motion range of 60.96 cm. Vertical loading is provided by a set of four actuators, one on each of the corners of the lower platen, and each actuator is capable of applying the full 14.715 MN force, so that the specimen can be placed anywhere on the platen surface. The top platen

was kept fixed, and loading was performed in displacement control mode for the current tests. The lowest displacement rate at which the lower platen can be raised is 0.02 mm/second, and this rate was used for the 0.7 m and 0.9 m specimens (strain rates of  $2.86 \times 10^{-5} \text{ s}^{-1}$  and  $2.22 \times 10^{-5} \text{ s}^{-1}$ , respectively). The MRS automatically tracks the load and platen movement throughout the loading process. Ideally, the specimens would have been placed directly on the lower platen, but given their weight, they had to be placed on a load cell for maneuvering with a forklift (Fig. 5). The implications of this for data analysis are discussed in Sect. 4.2.

### 3.3 3D Digital Image Correlation (3D-DIC) System

A 3D-DIC system from Trilion Quality Systems was used to monitor the deformation of the 0.7 m and 0.9 m specimens. 3D-DIC is a robust, non-destructive, non-contact optical technique by which the full-field displacement and strain fields across a specimen surface can be monitored in real time. The background and working principles of DIC can be found in numerous studies in literature and are therefore not discussed here in detail (Pan et al. 2009; Sutton et al. 2009; Munoz et al. 2016; Cheng et al. 2017; Xing et al. 2018; Tang et al. 2019). In simple terms, the

displacements and strain fields are obtained in DIC by tracking different regions or subsets on a specimen surface (in the form of digital images) as it deforms progressively during the loading process. A random speckle pattern acts as a carrier of the deformation information of the specimen surface (Pan et al. 2009; Schwartz et al. 2013). DIC basically locates subsets of the digital images in the deformed state with respect to their location in the reference/undeformed image. In 3D stereoscopic DIC systems, two cameras view the surface of the specimen. The camera system is calibrated (using a calibration plate) such that the relationship between raw and real space is known. Accuracy of this setup in “in-plane” direction is roughly 20  $\mu\text{m}/\text{m}$  and roughly 40  $\mu\text{m}/\text{m}$  in the “out-of-plane” direction (Trillion Quality Systems 2021).

The DIC setup employed 35 mm lenses (focal length) and 12 MP cameras, meaning that each picture had 12 million pixels (4096  $\times$  3000). The two cameras were placed on a steel bar, and their relative position, as well as the position of the 3D-DIC with respect to the specimen, was adjusted such that the entire specimen surface could be viewed by both the cameras. Before conducting the tests, an artificial random speckle pattern had to be created on the vertical surface to be monitored. This is an important requirement for 3D-DIC to operate. To create the speckle pattern, the block surface was first painted white, and then spray painted with black color under low nozzle pressure. This allowed relatively large speckles to be obtained so that there were at least 5 pixels across every speckle (recommended by Trillion Quality Systems for good results; Trillion Quality Systems 2020). The pixel size can be approximately determined as follows: for a 0.9 m block, there will be 3000 pixels over 900 mm, meaning that each pixel is 0.3 mm in size. A single speckle should therefore have a diameter of at least 1.5 mm. Many practice runs were made with different nozzle pressures to create speckles  $\geq 1.5$  mm prior to preparing the 0.7 m and 0.9 m blocks.

GOM Correlate software (GOM 2016) was employed for analyzing the 3D-DIC data, and a facet size and point distance of 16 pixels and 12 pixels, respectively, were used. Facet size stipulates the size of subsets (16 pixels  $\times$  16 pixels) to be compared in the deformed and reference image using statistical criteria, while the point distance (12 pixels) defines how far apart the center of the neighboring facets are located (Niu et al. 2016; Sjöberg et al. 2017). Typically, point distance is selected to be smaller than the facet size to ensure overlap between neighboring facets, which improves result accuracy (Malyszko et al. 2017; Mokhtari et al. 2019). Reducing the point distance improves resolution but has a dramatic effect on the computation time of GOM Correlate. To obtain a high resolution, a point distance of 12 pixels was selected as this is smaller than the default 15 pixel setting

of GOM Correlate and also because further reduction did not have any apparent effect on the calculated stress–strain curves.

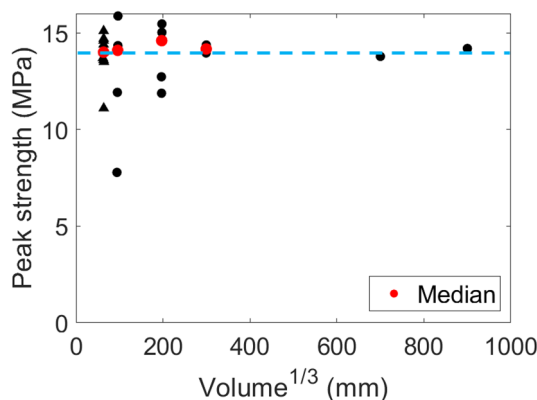
## 4 Size Effect Test Results

### 4.1 Peak Strengths

Figure 6 summarizes the results of this testing campaign. Median strengths are also presented for those specimen sizes on which multiple tests were conducted. It is evident that Texas Cream Limestone exhibits no size effect, at least over the range of specimen sizes and shape (width/height = 1) tested; it is possible that blocks with different width to height ratios may exhibit some size effect. Additionally, the median strength obtained from the UCS tests (Sect. 2) is similar to that obtained from the smallest cubes, suggesting the absence of any shape effect over this range of aspect ratios. This is in contrast to the typical trend where the compressive strength of a specimen increases as its aspect ratio is increased because a greater volume of the specimen comes under the influence of platen–rock friction generated confinement (Tang et al. 2000; Hemami and Fakhimi 2014; Al-Rkaby and Alafandi 2015; Gao et al. 2018). This is discussed further in Sect. 5.

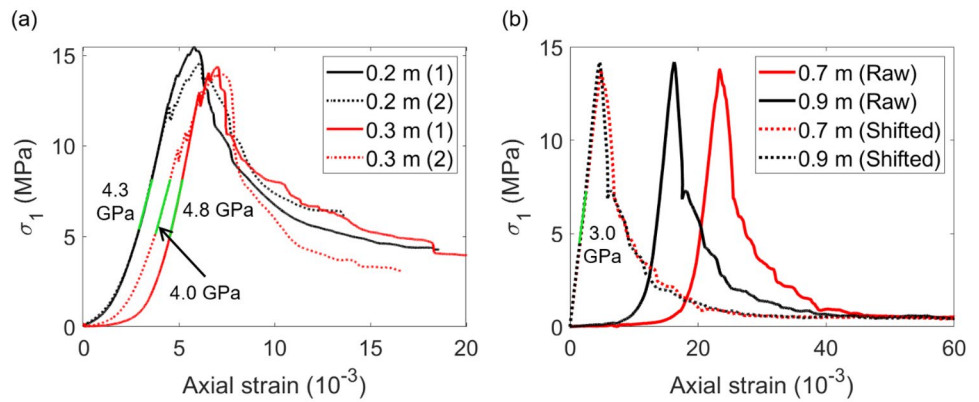
### 4.2 Stress–Strain Curves Derived from Loading System Data

Figure 7 shows global stress–strain curves obtained from the 0.2 m, 0.3 m, 0.7 m, and 0.9 m block tests. The strains



**Fig. 6** Peak unconfined strengths for all tested blocks. The volume of each specimen is based on the dimensions reported in Table. The median values are also shown in red for sizes on which multiple tests were conducted. The UCS results discussed in Sect. 2 are also added for completeness (datapoints indicated by triangles); since both cylindrical and cube shapes were considered,  $(\text{Volume})^{1/3}$  was used on the abscissa

**Fig. 7** **a** Representative axial stress–strain curve for two 0.2 m blocks and two 0.3 m blocks. **b** Raw and shifted axial stress–strain curves for the 0.7 m and 0.9 m blocks. The ‘shifted’ curves were derived from the ‘Raw’ curves by removing the initial non-linear sections and aligning the linear sections of the 0.7 m and 0.9 m specimens



were computed by simply dividing the system-derived platen movements by the specimen height and do not necessarily represent true rock strain. The extended non-linear sections at the start of some of the tests can be attributed to seating of the platens on the loading faces. Following this phase, a near-linear response can be observed, with the slopes of the stress–strain curves being consistent in both sets of tests (Fig. 7a and b). Once the peak strength is attained, all specimens exhibited a relatively brittle strength loss; this is expected, as the width to height ratio of these specimens is 1 (Mortazavi et al. 2009; Kaiser et al. 2011; Sinha and Walton 2018, 2021; Renani and Martin 2018).

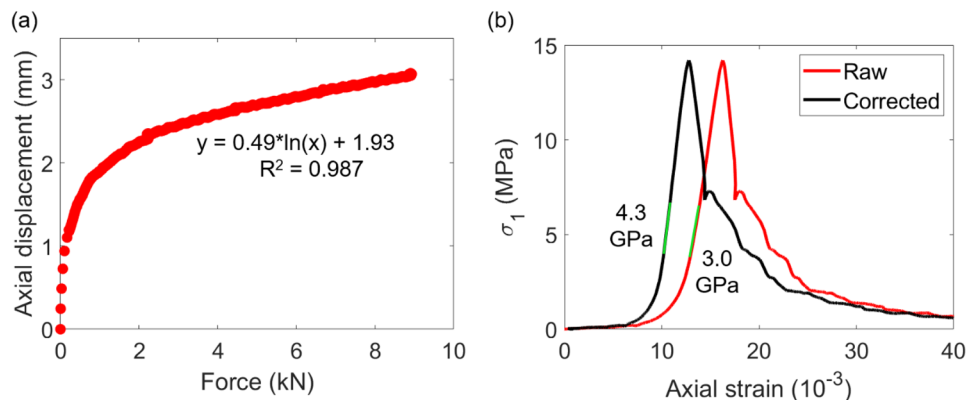
The slopes of the linear sections of the stress–strain curves (green segment in Fig. 7) would ideally represent the true Young’s modulus of the Texas Cream Limestone specimens. However, when the slopes were computed, values ranging from ~ 3 GPa to 4.8 GPa were obtained, which are much lower than those determined from the UCS tests (Table 1). There are two plausible reasons. The first is that this rock shows a dramatic size effect in Young’s modulus, but not in strength. This is unlikely, as studies that have recorded notable size effects on strength have typically only observed a modest (< 10%) decrease in elastic modulus from small to large specimens (Jackson and Lau 1990; Thuro et al. 2001; Darlington et al. 2011). The other possible explanation

is that the platen displacement measurements are not directly representative of the specimen deformation. In other words, the movements recorded by the testing machines include contributions from sources other than the limestone specimen deformation.

The unstressed reference frame in the MRS enables removal of the platen deflection from the control command so that any deflection of the platens is eliminated in the specimen displacement control. Additionally, the frame has very high stiffness (0.37 GN/m), meaning that the only system component that could incur substantial deformation in addition to that incurred by the rock specimens themselves is the load cell below the blocks. A compression test was conducted on just the load cell, and the corresponding load–displacement data is shown in Fig. 8a. A simple approach to correct the global stress–strain response of the 0.9 m block is to fit a curve to the load–displacement data of the load cell and then subtract the displacement contribution from the load cell at different load levels from the total LVDT displacement. The following equation was found to fit the load–displacement data of the load cell data with an  $R^2$  of 0.99:

$$Disp(mm) = 0.49 * \ln(loadinkN) + 1.93. \tag{1}$$

**Fig. 8** **a** Displacement–force behavior of the load cell. **b** Raw and corrected (considering the displacement of the load cell) stress–strain curve for the 0.9 m block



The MRS-measured load–displacement curve for the 0.9 m block was taken, and the corresponding displacement contribution of the load cell was subtracted by inputting the load levels into Eq. 1 and subtracting it from the total displacement. The original and corrected stress–strain curves are shown in Fig. 8b. When applying this approach, the modulus increased from 3.0 GPa to 4.3 GPa (43.3% increase), but the modulus is still much lower than the mean value indicated in Table 1.

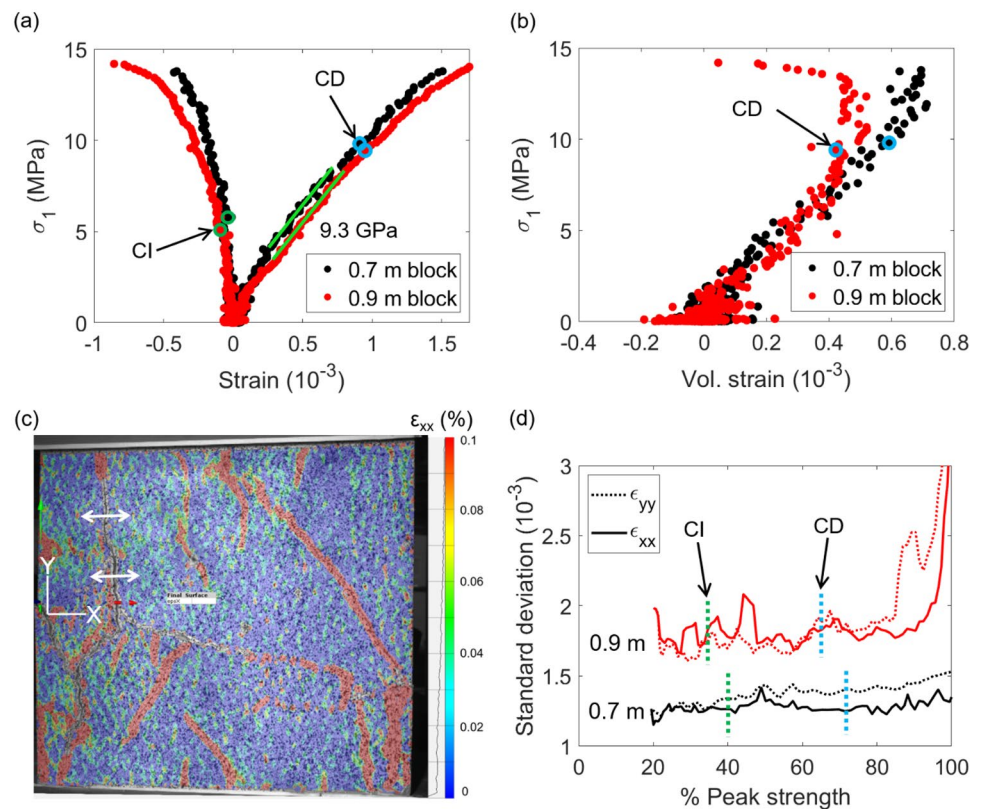
Although we cannot provide a definitive answer for why this correction approach did not provide realistic Young’s modulus values, we believe this discrepancy (measured strain versus true strain) is associated with the stiffness influences of the multiple contacts within the platen–block–load cell system. In other words, the low stiffness interfaces between the different components lower the overall stiffness of the system, but it is not straightforward to mathematically omit the stiffness contributions of these interfaces. Similar discrepancies were also observed by Abdelaziz and Grasselli (2021) when comparing Young’s modulus of Stanstead Granite derived from different testing machines and by Alejano et al. (2020, 2021) when comparing UCS stress–strain curves obtained from LVDTs and strain gauges for Olkiluoto gneiss and Blanco Mera granite specimens. The lower moduli from the 0.2 m, 0.3 m, and 0.7 m block tests can be explained using the same reasoning, as multiple platens had to be used for the 0.2 m and 0.3 tests to raise the specimen.

It is noted that the moduli of 0.2 m and 0.3 m blocks and 0.7 m and 0.9 m blocks are similar for specimens loaded within a given test setup but differ by  $\sim 1$ –1.5 GPa between test setups (Fig. 7a and b). This is likely because the loading arrangement is the same within each group, further corroborating the system stiffness explanation for the discrepancies between Young’s modulus values obtained in different sets of tests.

### 4.3 3D-DIC Analysis

Given the issue of determining true rock strain directly from the MRS data, the X and Y strains (i.e. individual datapoints of the strain field) obtained from the 3D-DIC analysis were averaged over the entire specimen surface for the 0.7 m and 0.9 m specimens; the average strains are plotted against vertical stress in Fig. 9a. 3D-DIC gives the true rock specimen strain as it only tracks deformation on the specimen itself, and neglects any deformation of the loading system. For the 0.9 m specimen, a rectangular region extending 0.35 m from the right margin was omitted from this analysis due to significant noise in the strain field associated with a lighting issue (see Appendix B for more details). The DIC analysis could not be extended into the post-peak, as the speckle pattern was lost due to surficial specimen spalling. The slope of the linear portion of the axial stress–axial strain curve is  $\sim 9.3$  GPa, which is close to the average elastic modulus obtained

**Fig. 9** **a** Stress–strain curves for the 0.7 m and 0.9 m blocks obtained from the 3D-DIC analysis. **b** Axial stress–volumetric strain curve for the 0.7 m and 0.9 m blocks obtained from the 3D-DIC analysis. **c** Minor principal strain field in the 0.7 m specimen after failure. **d** Standard deviation of the major ( $\epsilon_{yy}$ ) and minor ( $\epsilon_{xx}$ ) principal strain field as a function of % peak strength. A moving average technique considering a window size of five datapoints was used to smoothen the strain-field heterogeneity





from UCS tests (10.9 GPa, see Table 1). The crack damage (CD) and crack initiation (CI) thresholds were also determined as the point of non-linearity in the axial stress–axial strain curve and axial stress–lateral strain curve, respectively (Martin and Chandler 1994; Diederichs 2007; Diederichs and Martin 2010). CI threshold marks the onset of extensile microcracking in a rock specimen and while CD corresponds to the onset of microcrack interaction and coalescence and is more generally known as the yield point (Diederichs and Martin 2010; Cai 2010).

Figure 9b shows the volumetric strain as a function of axial stress and was computed using the equation  $\epsilon_v = 2\epsilon_{xx} + \epsilon_{yy}$  (refer to Fig. 9c for the coordinate system used in GOM Correlate). GOM Correlate only provides displacements in the out-of-plane direction, but not strains, as there is no base length associated with the out-of-plane direction. It can be seen that the volumetric strain reversal occurred after the point of axial strain non-linearity under unconfined conditions; although these two points are known to generally be coincident for low porosity crystalline rocks, such a delay in the onset of absolute dilatancy relative to the onset of yield has previously been observed in a different porous sedimentary rock (Walton et al. 2017).

The minor principal strain values ( $\epsilon_{xx}$ , which is approximately equivalent to  $\epsilon_{33}$  in this case) are more sensitive to the formation of axial microcracks than the other strain components and were therefore employed for further analysis (Shirole et al. 2020; Sinha et al. 2021). The major principal strain ( $\epsilon_{yy}$ , which is approximately equivalent to  $\epsilon_{11}$ ) was also analyzed in this case as axial microcracking is not the only inelastic deformation process in porous rock (Wong and Baud 2012). Diederichs (1999) and Lan et al. (2010) previously demonstrated using micromechanical models how the grain-scale heterogeneity in rock stress increases with increasing specimen damage. With the full-field strains computed, it was possible to visualize this heterogeneity in terms of strains rather than stresses.

Figure 9d shows the standard deviation of the major and minor principal strains in the 0.7 m and 0.9 m specimens as a percentage of peak strength. Shirole et al. (2020) discussed how heterogeneity in  $\epsilon_{33}$  increases after attaining CI and CD in the context of three low porosity rocks due to formation and opening of microcracks oriented parallel/sub-parallel to the specimen axis. Such a behavior was not observed in the Texas Cream Limestone specimens, where strain heterogeneity was constant up to ~90% of peak strength (Fig. 9d). An important point to consider here is the area over which each strain datapoint is computed, also called ‘gauge length’ (Shirole et al. 2020), as it controls the heterogeneity in the strain field. As gauge length is increased, the strain field becomes homogeneous due to greater areal averaging (relative to the scale of micro-damage). In our case, the strain datapoints

from GOM Correlate were spaced at ~2.75 mm (a function of point distance) for the 0.9 m specimen, meaning that each datapoint represented an area of 2.75 mm × 2.75 mm (gauge length = 2.75 mm). Shirole et al. (2020) tested gauge lengths varying from 1 to 128 mm for three low porosity rocks and illustrated a  $\epsilon_{33}$  heterogeneity reduction with increasing gauge lengths. Since our gauge length is closer to the lower bound, Fig. 9d can be best compared to the 1 mm gauge length results of Shirole et al. (2020). In contrast to  $\epsilon_{xx}$ , perturbations in  $\epsilon_{yy}$  strain field started to increase as early as 40% peak strength, which is opposite to what one would observe in low porosity brittle rocks (Shirole et al. 2020); the implication of this finding is discussed later under Sect. 5.2. No specific reason for the small offset in the standard deviation magnitude in the 0.7 m and 0.9 m specimens is known; this may be due to geological variability between the two specimens, or slight differences in their speckle patterns. In either case, the relationship between the strain variations in X and Y direction are more meaningful to the current discussion than the absolute difference between the two specimens.

#### 4.4 Fracture Patterns

Figure 10 shows the 0.7 m specimen at different stages of loading: (1) damage initiated in the form of surficial spalling on all four faces; (2) two opposite faces collapsed completely, leading to the formation of an asymmetric core; (3) with continued loading, the core became more symmetric; (4) fracturing continued to propagate deeper into the core. For this specimen (as well as the 0.9 m specimen), the peak strength was attained as soon as the surficial spalling process visibly initiated. Although the formation of a core was evident in these tests, it is important to note that these cores do not possess any substantial load carrying capacity (refer to the low residual stress level in Fig. 7b). A different behavior might be expected in specimens with different width to height ratios where the cores are typically more confined and result in elevated residual stress levels (Mortazavi et al. 2009; Esterhuizen et al. 2010; Sinha and Walton 2018). Similar hour-glassing was observed in the smaller specimens as well; Fig. 11 shows the states of 0.2 m and 0.3 m specimens after the termination of testing.

## 5 Discussion

### 5.1 Stress–strain response

For both the 0.2 m and 0.3 m specimens (Fig. 7), the overall stress–strain response is noted to be fairly consistent in the pre- and the post-peak regime. Even more remarkable is the resemblance in the 0.7 m and 0.9 m stress–strain

**Fig. 10** Fracture evolution in the 0.7 m specimen during the loading process. Peak was attained immediately after the ‘surficial spalling’ stage

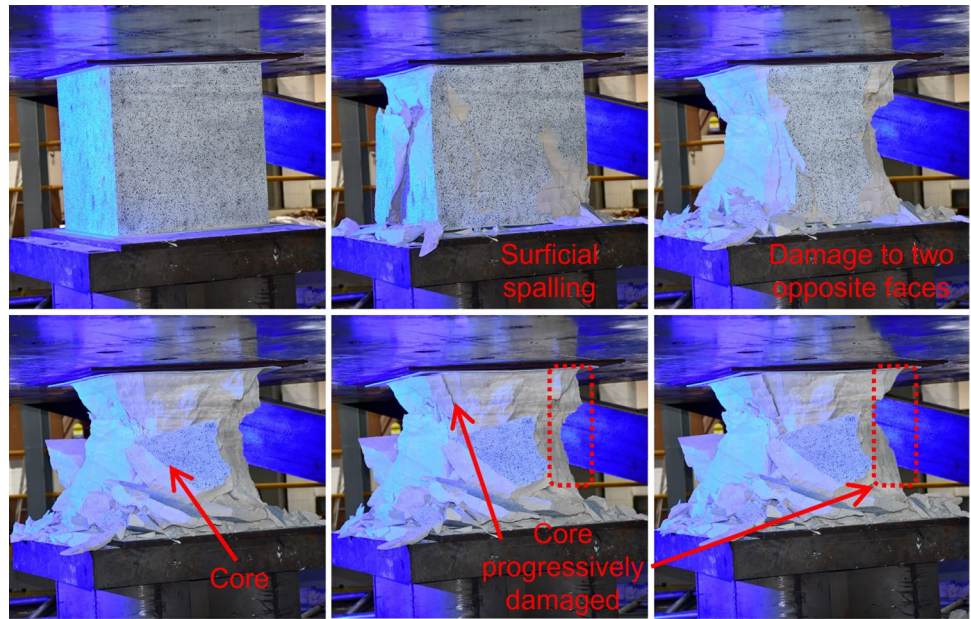
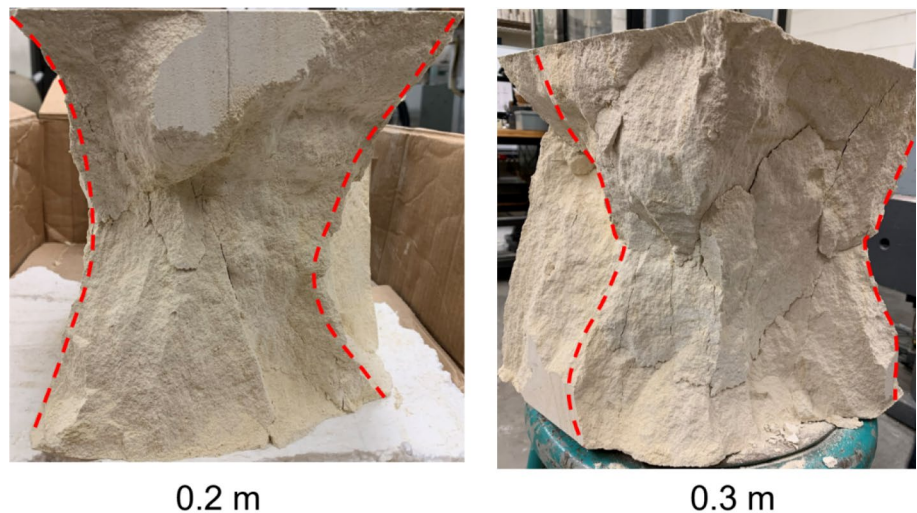


**Fig. 11** Hourglass fracture pattern (marked by broken red lines) observed for the 0.2 m and 0.3 m specimens post-testing



response (dotted lines in Fig. 7b) after the two curves were shifted to omit the initial non-linear segments. The consistency in test results confirms two propositions: (1) the faces of the specimens were adequately parallel and were loaded uniformly by the testing machines; if the extent of non-parallelism was significant, then some edge(s) of the specimen would have fractured preferentially, yielding dissimilar stress–strain curves; (2) Texas Cream Limestone exhibits no notable size effect for blocks ranging from 0.1 m to 0.9 m edge length.

The residual strengths of 0.7 m and 0.9 m specimens are  $\sim 0.5$  MPa, which is significantly smaller than that of 0.2 and 0.3 m specimens. This discrepancy could be attributed to the different test setups, or there could be

an absolute size effect on the residual strengths. Regarding the former explanation, it is possible that the stresses may have reduced further with further strain ( $> 2\%$ ) in the 0.2 m and 0.3 m specimens, but this was not done due to the machine reaching its maximum displacement capacity.

## 5.2 Peak Strength Results and Comparison to Data From Literature

We have seen in Fig. 6 that Texas Cream Limestone exhibits no appreciable size effect. Additionally, a comparison of the strengths of cubic (length/width  $\sim 1$ ) and cylindrical specimens (length/diameter  $> 2$ ) indicates no apparent shape

effect, consistent with the test results on marble and tuff presented by Tuncay and Hasabcebi (2009).

Another observation that can be made from Fig. 6 is that the variability in strength reduces with an increase in the examined rock volume up to 300 mm edge length (the standard deviations of peak strength for 100 mm, 200 mm, and 300 mm edge lengths are 3.14 MPa, 1.55 MPa and 0.29 MPa, respectively). We interpret the variability in mechanical properties to be greater at smaller sizes because of the potential for local geological heterogeneity to exert significant control on the overall failure process and/or greater potential for end effects and geometrical tolerances to influence material behavior. If the variability of mechanical properties is considered for identification of the representative elementary volume (e.g., per Farahmand et al. 2018), then the 300 mm edge length blocks can be interpreted to be of a size similar to the representative elementary volume for Texas Cream Limestone. Although it is not possible to draw definitive conclusions for edge lengths > 300 mm from only two such tests, the fact that the results of 0.7 m and 0.9 m (Fig. 7b) are both similar to one another and to the median values obtained from smaller specimens is consistent with the interpretation that the representative elementary volume corresponds to an edge length on the order of 300 mm.

To evaluate the size effect in sedimentary rocks more broadly, data from prior studies were compiled and are presented in Fig. 12 (see Appendix C for supporting data). To prepare Fig. 12, the empirical equation proposed by Hoek and Brown (1980) was considered:

$$UCS_d = UCS_{50} \left( \frac{d}{50} \right)^\beta, \quad (2)$$

where  $UCS_d$  and  $UCS_{50}$  are UCS of specimens with diameter of  $d$  and 50 mm, respectively, and  $\beta$  is a constant. Equation 2 was fit to the raw UCS versus diameter data from each study to obtain estimates of  $UCS_{50}$  (termed here as ‘fit parameter  $\alpha$ ’) and  $\beta$ . The so-called “reverse scale-effect” portion of the curve, i.e., the section where strength increases with diameter (see Fig. 1), was omitted from the curve fitting process, as this phenomenon occurs in small sized specimens due to mechanisms separate from those that can be represented by Eq. 2 (Vutukuri et al. 1974; Quiñones et al. 2017). Caution should be exercised when employing small exploration cores to obtain  $UCS_{50}$  using Eq. 2 as it can potentially lead to downgrading of an already downgraded strength.

Data for cubic specimens from the current study and Celik (2017) were also added to this analysis, and the equivalent diameter of each square cross section was used for purposes of comparison. The  $\beta$  parameter obtained from this curve fitting process is shown in Fig. 12a.  $\beta$  mathematically describes how rapidly the normalized UCS value drops with increasing specimen diameter. Larger negative values of  $\beta$  correspond to more significant size effects. Porosity values for each of the rocks were taken directly from each study when available or from a different study using the same rock (see Appendix C for details). In the cases of Burrington Oolite and Clifton Down Limestone (Hawkins 1998), the porosity value was estimated based on a curve fit (Eq. 3) to the UCS-porosity data presented by Hawkins (1998):

$$UCS = 426.07 Porosity^{-0.994}. \quad (3)$$

While the mineralogical details of these rocks may vary based on diagenetic processes (e.g., quartz vs. calcite cement, etc.), porosity appears to be a major factor influencing the extent of each rock’s size effect ( $\beta$ ). Overall, the

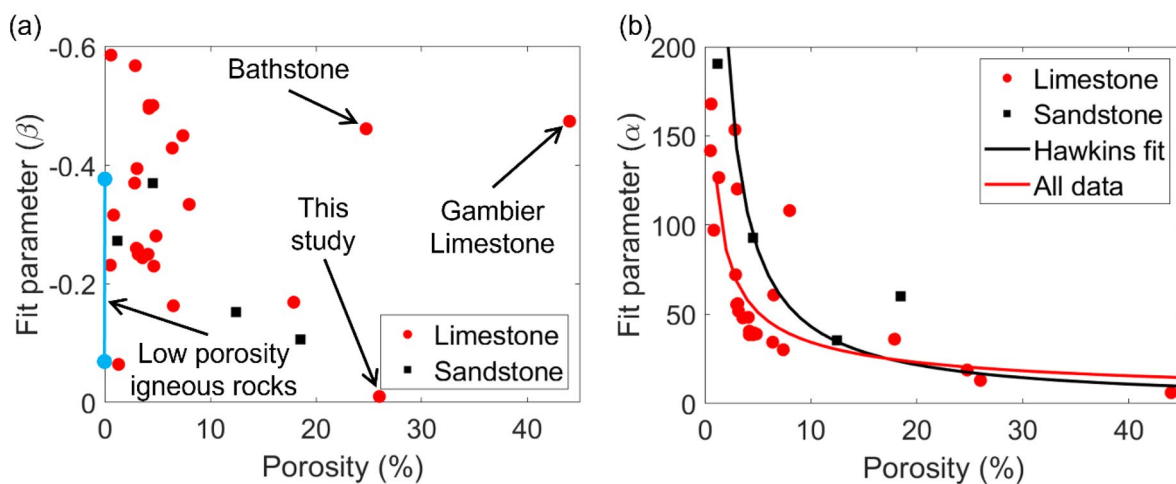


**Fig. 12** **a**  $\beta$  versus porosity data from literature.  $\beta$  for low porosity igneous rocks is also indicated in this figure. **b** Power fit to  $\alpha$  versus porosity data



data indicate that increased porosity tends to dampen the size effect. This has a significant practical implication, in that the use of Hoek and Brown (1980) equation to apply a scale adjustment in high porosity rocks may result in an underestimation of rock strength at the field scale and lead to overdesign of engineered structures. Some additional discussion on the behavior of the two outliers, Bathstone (Hawkins 1998) and Gambier Limestone (Zhai et al. 2020), can be found in Appendix C. Porosity has a well-known influence on  $UCS_{50}$  ( $\alpha$ ; Chang et al. 2006; Wong and Baud 2012), and this was also observed in the current study (Fig. 12b).

Figure 12a also shows the range of  $\beta$  for low porosity, hard igneous rocks. The range of  $\beta$  for low porosity hard igneous rocks was calculated by fitting Eq. 2 to the data from Nishimatsu et al. (1969), Hoek and Brown (1980), Jackson and Lau (1990), and Walton (2018), and then selecting the smallest and largest fit parameter  $\beta$ . The bounds on  $\beta$  for igneous rocks, along with the overall best fit from Hoek and Brown (1980), is presented in Fig. 13. Notably, many of the low porosity sedimentary rocks demonstrate a greater size effect than igneous rocks, which appears to contradict Cunha's (1990) explanation of size effects based on material heterogeneity. With that said, low porosity sandstones may have some clay fraction, and the stiffness contrast between clay and quartz (modulus of clay = 6.6 MPa (Prat et al. 1995; Strózyk and Tankiewicz 2016) and modulus of quartz = 94.5 GPa (Bass 1995)) could explain the larger size effect in comparison to granites (modulus of biotite mica = 33.8 GPa and modulus of plagioclase and quartz ~ 95 GPa; Bass 1995). Limestone composed entirely of  $CaCO_3$  can have structural or geometric heterogeneity (different grain shapes and sizes and/or presence of ooids, fossils; Folk 1959; Lan et al. 2010), and the probability of forming critical fractures early on in the compressive loading process could be higher in larger specimens.

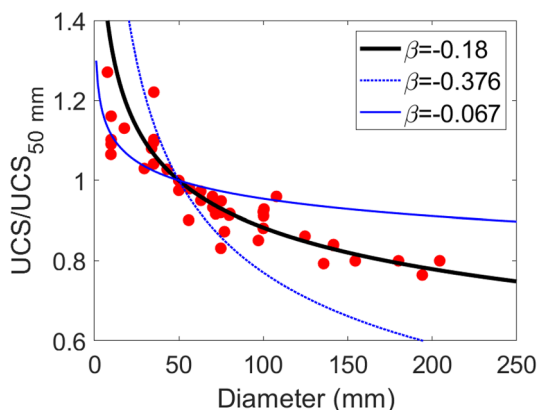


**Fig. 13** Normalized UCS data versus diameter for low porosity igneous rocks with upper and lower bound of  $\beta$

For porous rocks, it is hypothesized that through pore collapse mechanisms, more deformation can be accommodated without the need to dilate by extensile cracking mechanisms, thus resulting in a limited size effect (Elliot and Brown 1985; Wong and Baud 2012; Walton et al. 2015). The 3D-DIC analysis on Texas Cream Limestone (Fig. 9c) indicates a net positive volumetric strain (contraction) even when the specimens attained their respective peak strengths (the trend is however dilative). Additionally, the lack of  $\epsilon_{xx}$  heterogeneity and early initiation of  $\epsilon_{yy}$  heterogeneity (Fig. 9d) indicates limited formation and lateral dilation of microcracks, and deformation was interpreted to be through pore collapse in the axial direction. All these observations support our hypothesis regarding the lack of size effect in Texas Cream Limestone. More study is needed to better understand the role that porosity plays in controlling the size effect from a micromechanical perspective.

## 6 Conclusions

In this study, unconfined compression tests were conducted on Texas Cream Limestone blocks ranging in edge lengths from 0.1 to 0.9 m to investigate size effects in porous rocks. Geomechanical characterization of the rock was completed prior to conducting the tests on the cube specimens using conventional rock mechanics tests (compression and indirect tensile tests on cylindrical samples). Additionally, a 3D digital image correlation system was employed to monitor changes in the displacement field as a function of applied load for two of the largest specimens. The conventional tests revealed that Texas Cream Limestone has a UCS of 13.9 MPa, an elastic modulus of 10.9 GPa, and an indirect tensile strength of 1.7 MPa. The porosity of the rock was also determined to be ~26% using theoretical calculations, which is also consistent with literature.

Contrary to the size effect relationship of Hoek and Brown (1980), Texas Cream Limestone showed essentially no size effect on strength for the entire range of specimen sizes tested. Data from prior studies on sedimentary rocks were compiled, and a decline in size effect was noted with increasing porosity, with two notable outliers. It was hypothesized that the reason for the reduced size effect in porous rocks is due to the ability of such rocks to accommodate more deformation through pore collapse mechanisms rather than having to dilate via extensile fracturing mechanisms. Perturbations in minor and major principal strain fields obtained from the 3D-DIC analysis, which physically represent stress heterogeneity, seem to support this hypothesis. Specifically, minimal changes in minor principal strains (lateral direction) were observed until the specimens were



loaded to ~90% of peak strength, while variations in major principal strain field (axial or loading direction) initiated much earlier. The former observation suggested that limited extensile crack formation and opening occurred, while the latter observation was interpreted to be associated with pore collapse mechanisms.

## Appendix A: Geometrical Details of Test specimens

The mean and standard deviation of the heights of the 0.2–0.9 m specimens are listed in Table A1, while the mean dimensions in three perpendicular directions are listed in Table A2. The 0.1 m specimens were only measured once in the three perpendicular directions. While congruence in height measured along different vertical faces does not imply parallelism for the entirety of the loading surfaces (i.e. central portion versus edges), we believe it is reasonable to assume the surfaces to be planar when cut using a saw. Accordingly, the dimensions measured along the edges are considered to be representative of the entire loading surface.

The mean dimensions along the x, y, and z directions are most dissimilar for the 0.1 m specimens (Table 3). The reason is that the 0.1 m specimens were saw-cut from one 0.2 m block and then ground until two opposite faces were parallel. This grinding process and minor errors in subdividing the 0.2 m block led to the variation in the edge lengths. In any case, the width to height ratio of all 0.1 m specimens was within the interval [0.98, 1.06], and this change in aspect ratio is unlikely to affect the strengths in any meaningful way (Du et al. 2019).

The ASTM suggested method covering the preparation of UCS specimens (ASTM 4543-85, 2001) requires ends to be flat to  $\pm 0.025$  mm and not depart from perpendicularity to the longitudinal axis by more than 0.25 degrees (or 0.22 mm in 50 mm). It is noted here that the ASTM specifications were developed for smaller cylindrical specimens and possibly represent a lower bound (in terms

**Table A2** Mean dimension of each test specimen

Specimen name	Specimen #	Dimensions in mm (x, y, z)—loading along z
0.1 m specimens	Specimen 1	92.89×95.98× 93.32
	Specimen 2	96.99×96.62× 95.78
	Specimen 3	95.56×97.23× 96.12
	Specimen 4	96.63×97.14× 91.50
	Specimen 5	97.05×96.25× 97.46
0.2 m specimens	Specimen 1	197.48×195.63×196.82
	Specimen 2	197.53×197.20×197.59
	Specimen 3	197.67×196.89×197.39
	Specimen 4	197.02×197.43×197.81
	Specimen 5	196.01×196.46× 197.38
0.3 m specimens	Specimen 1	300.1×298.5× 300.0
	Specimen 2	295.5×298.1× 300.1
0.7 m specimens	Specimen 1	698×696× 697.8
0.9 m specimens	Specimen 1	899×898× 897.8

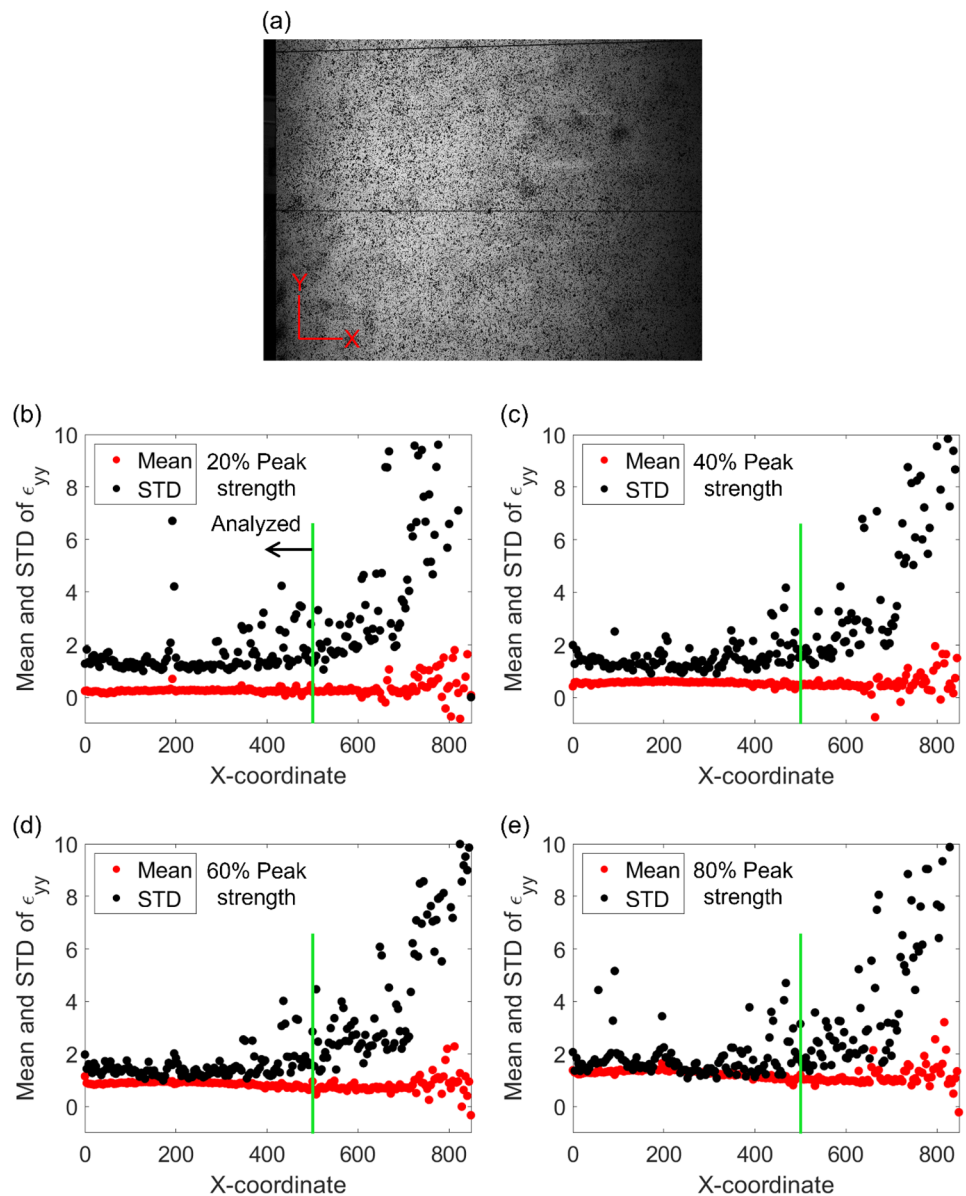
of stringency) of specimen requirement (Cvitanović et al. 2015). The flatness of the 0.2–0.9 m specimens were not measured explicitly, but if the variability in specimen size (Table 2) is normalized with respect to the edge length, then all values are lower than the corresponding recommended value in Cvitanović et al. (2015). In terms of parallelism of the loading surfaces, if  $2 \times \text{variability} / \text{mean edge length}$  is computed for all specimens in Table 2, then the value ranges from [0.0005, 0.0027]; the corresponding ASTM requirement is 0.0044. All specimens, therefore, satisfy the parallelism requirement of ASTM, but some of the specimens exceed the stricter ISRM stipulations (0.001 radians or 0.05 mm in 50 mm; Fairhurst and Hudson 1999). In any case, the fact that highly consistent stress–strain curves and fracture patterns were obtained (as reported in Sect. 4) provides confidence in the test results.

**Table A1** Mean and standard deviation of the height of each specimen

0.2 m specimens—measured using Vernier caliper	Specimen 1 (mm)—12 measurements	196.82 ± 0.11
	Specimen 2 (mm)—12 measurements	197.59 ± 0.10
	Specimen 3 (mm)—12 measurements	197.39 ± 0.05
	Specimen 4 (mm)—12 measurements	197.81 ± 0.09
	Specimen 5 (mm)—12 measurements	197.38 ± 0.18
0.3 m specimens—measured using tape	Specimen 1 (mm)—12 measurements	300.0 ± 0.3
	Specimen 2 (mm)—12 measurements	300.1 ± 0.4
0.7 m specimens—measured using tape	Specimen 1 (mm)—12 measurements	697.8 ± 0.7
0.9 m specimens—measured using tape	Specimen 1 (mm)—12 measurements	897.8 ± 0.7

The 0.1 m specimen was not measured multiple times as it was ground at Colorado School of Mines

**Fig. 14** **a** Raw image from one of the 3D-DIC camera at a load level corresponding to 20% peak strength. Mean and standard deviation of  $\epsilon_{yy}$  strain field computed within rectangular strips 0.75 mm wide across the entire width of the specimen at **b** 20% peak strength, **c** 40% peak strength, **d** 60% peak strength, and **e** 80% peak strength. X-coordinate is the center point of the moving rectangular window



## Appendix B: Adjustment in Strain Calculation due to Lighting Issues

During the calculation of strain heterogeneity, significant noise was observed in the strain field generated by GOM Correlate along the right edge of the 0.9 m specimen. The raw images captured by 3D-DIC were revisited, and some issues with lighting were identified. In particular, about  $\sim 0.35$  m of the specimen right side was found to be darker than the rest of the image (Fig. 14a). This issue was not present in the 0.7 m specimen images, and the

lighting was consistent across the entire surface. To filter out the noise in the DIC data, the mean and standard deviation of  $\epsilon_{yy}$  was computed within rectangular bins that were 0.75 mm wide (3 pixels) and spanned the entire specimen height. The results at 20%, 40%, 60%, and 80% peak strength are plotted against the X-coordinate of the bin midpoints in Fig. 14b–e. Since the standard deviation of the  $\epsilon_{yy}$  strain started to fluctuate dramatically in the rightmost  $\sim 350$  mm region (Fig. 14b–e), that portion was omitted while preparing Fig. 9.

**Table C1** Data (and references) used for plotting Fig. 12

Rock name	References	$\alpha$ (MPa)	$\beta$	$R^2$	Porosity (%)	References
Pilton Sandstone	Hawkins (1998)	190.42	- 0.27	0.93	1.34	Hawkins and McConnell (1991)
Clifton Down Limestone	Hawkins (1998)	120.27	- 0.39	0.94	3.06	Eq. (3)
Purbeck Limestone	Hawkins (1998)	108.16	- 0.33	0.91	8.0	Marker (2015)
Pennant Sandstone	Hawkins (1998)	92.87	- 0.37	0.94	4.57	Hackston and Rutter (2016)
Bathstone	Hawkins (1998)	18.78	- 0.46	0.88	24.5	Marker (2015)
Burrington Oolite	Hawkins (1998)	153.47	- 0.37	0.98	2.84	Eq. (3)
Hollington Sandstone	Hawkins (1998)	35.25	- 0.15	0.90	12.45	Baychev (2018)
Alfas Stone	Kaklis et al. (2015)	36.06	- 0.17	0.99	17.92	Nomikos et al. (2020)
Gosford Sandstone	Masoumi et al. (2016)	60.29	- 0.106	0.98	18.5	Masoumi et al. (2016)
Gambier Limestone	Zhai et al. (2020)	6.09	- 0.47	0.99	44	Khishvand et al. (2016)
Azarshahr Wavy Red	Jamshidi et al. (2016)	30.15	- 0.45	0.94	7.41	Jamshidi et al. (2016)
Azarshahr Walnut	Jamshidi et al. (2016)	56	- 0.26	0.96	3.10	Jamshidi et al. (2016)
Azarshahr Yellow	Jamshidi et al. (2016)	39.56	- 0.23	0.97	4.65	Jamshidi et al. (2016)
Azarshahr Silver	Jamshidi et al. (2016)	51.83	- 0.25	0.94	3.17	Jamshidi et al. (2016)
Atashkooch White	Jamshidi et al. (2016)	38.58	- 0.50	0.93	4.20	Jamshidi et al. (2016)
Abasabad Light Cream	Jamshidi et al. (2016)	39.01	- 0.28	0.81	4.86	Jamshidi et al. (2016)
Abasabad White	Jamshidi et al. (2016)	38.58	- 0.50	0.94	4.53	Jamshidi et al. (2016)
Abyar White	Jamshidi et al. (2016)	48	- 0.24	0.96	3.58	Jamshidi et al. (2016)
Dareh Bokhari Cream	Jamshidi et al. (2016)	34.41	- 0.43	0.88	6.40	Jamshidi et al. (2016)
Atashkooch Cream	Jamshidi et al. (2016)	40.56	- 0.49	0.98	4.2	Jamshidi et al. (2016)
Firuzkuh Chocolate	Jamshidi et al. (2016)	55.57	- 0.26	0.99	3.0	Jamshidi et al. (2016)
Firuzkuh Cream	Jamshidi et al. (2016)	48.32	- 0.25	0.85	4.10	Jamshidi et al. (2016)
Travertine (TD)	Celik (2017)	72.19	- 0.57	0.38	2.90	Celik (2017)
Limestone (LF)	Celik (2017)	60.85	- 0.16	0.60	6.50	Celik (2017)
Limestone (LY)	Celik (2017)	97.18	- 0.32	0.51	0.85	Celik (2017)
Limestone (LI)	Celik (2017)	141.74	- 0.23	0.87	0.53	Celik (2017)
Limestone (LS)	Celik (2017)	167.93	- 0.59	0.97	0.59	Celik (2017)
Texas Cream Limestone	This study	12.98	- 0.01	0.51	26	This study

### Appendix C: Discussion on the Two Outliers: Gambier Limestone and Bathstone

The data used to develop Fig. 12 are presented in Table 4. With respect to  $\beta$ , there are two notable outliers—Gambier Limestone and Bathstone. The exact reason why  $\beta < -0.4$  for these two rocks is not obvious. Gambier Limestone is reported to have ~44–50% porosity and is composed of 98% calcite (Khishvand et al. 2016; Zhai et al. 2020; Armstrong et al. 2021). It is hypothesized that such a homogeneous, high porosity rock can exhibit size effect if the pore size distribution itself is playing a role in the failure process (i.e. the volumetric proportion of larger pores is not attaining a constant value over the range of specimen sizes considered). This is somewhat evident in Fig. 1, where Gambier Limestone attains its maximum UCS at 119 mm size that is significantly larger than what is typical for most

rock types (40–60 mm; Kong et al. 2021). Pores can act as crack arrestors or stress concentrators; in this case, it is possible that the pores interacted with the surface to lead to premature failure in the < 119 mm diameter specimens and continued to play a role in the failure process through internal mechanisms (e.g., stress concentrating around larger pores, crack initiation) in the larger specimens. The fact that larger pores can lower material strength has been illustrated by Biao et al. (2017) and Li et al. (2020) using composites. Khishvand et al. (2016) also recently reported pore diameters as large as 0.8 mm for Gambier Limestone. The same reasoning may or may not be applicable to Bathstone that has a porosity of 23–26% (Marker 2015), and there could also be an interaction between the pores and its oolitic structure (Elliot and Brown 1985). It is interesting, however, that the UCS of Bathstone drops by 25.7% between 54 and 74 mm diameter and only by 15% between 74 and 150 mm diameter.

**Acknowledgements** The authors thank Thomas M Barczak, Earth Mechanics Institute at Colorado School of Mines (Bruce Yoshioka, Brent Duncan and Thyagarajan Muthu Vinayak) and NIOSH for assisting with the tests.

**Funding** The research conducted for this study was primarily sponsored by the Alpha Foundation for the Improvement of Mine Safety and Health, Inc. (ALPHA FOUNDATION) under Grant Number AFC820-52. Additional funding was obtained from National Institute for Occupational Safety and Health (NIOSH) under Grant Number 200–2016-90154.

**Data Availability** The data that support the findings of this study are available from the corresponding author, [Sankhaneel Sinha], upon reasonable request.

**Code Availability** Not applicable.

## Declarations

**Conflict of Interest** There is no conflict of interest.

## References

- Abdelaziz A, Grasselli G (2021) How believable are published laboratory data? A deeper look into system-compliance and elastic modulus. *J Rock Mech Geotech Eng* 13(3):487–499
- Alejano LR, Arzúa J, Estévez-Ventosa X, Suikkanen J (2020) Correcting indirect strain measurements in laboratory uniaxial compressive testing at various scales. *Bull Eng Geol Env* 79(9):4975–4997
- Alejano LR, Estévez-Ventosa X, González-Fernández MA, Walton G, West IG, González-Molano NA, Alvarillos J (2021) A method to correct indirect strain measurements in laboratory uniaxial and triaxial compressive strength tests. *Rock Mech Rock Eng* 54(6):2643–2670
- Al-Rkaby AH, Alafandi ZM (2015) Size effect on the unconfined compressive strength and Modulus of elasticity of limestone rock. *Electron J Geotech Eng* 20(12):1393–1401
- Armstrong RT, Lanec Z, Mostaghimi P, Zhuravljov A, Herring A, Robins V (2021) Correspondence of max-flow to the absolute permeability of porous systems. *Phys Rev Fluids* 6(5):054003
- ASTM D7012-04 (2004) Standard test method for compressive strength and elastic moduli of intact rock core specimens under varying states of stress and temperatures. West Conshohocken, USA: ASTM International
- ASTM D3967-16 (2016) Standard test method for splitting tensile strength of intact rock core specimens. West Conshohocken, PA
- ASTM D4543-85 (2001) Standard practices for preparing rock core specimens and determining dimensional and shape tolerances. D4543. West Conshohocken, PA: American Society for Testing and Materials
- Bandis S (1980) Experimental studies of scale effects on shear strength, and deformation of rock joints. PhD dissertation, University of Leeds
- Baecher GB, Einstein HH (1981) Size effect in rock testing. *Geophys Res Lett* 8(7):671–674
- Barczak TM (2000) NIOSH safety performance testing protocols for standing roof supports and longwall shields. In: Proceedings of the New Technology for Coal Mine Roof Support, Pittsburgh, PA: US Department of Health and Human Services, Public Health Service, Centers for Disease Control and Prevention, National Institute for Occupational Safety and Health, DHHS (NIOSH) Publication, no. 2000–151 pp 207–221
- Barczak T (2005) An overview of standing roof support practices and developments in the United States. In: Proceedings of the Third South African Rock Engineering Symposium, Johannesburg, South Africa pp 301–334
- Barton N (1990) Scale effects or sampling bias? In: Proceedings of international workshop scale effects in rock masses. Balkema, Rotterdam, pp 31–55
- Bass JD (1995) Elasticity of minerals, glasses, and melts. *Mineral Physics and Crystallography: A Handbook of Physical Constants* 2:45–63
- Baychev TG (2018) Pore space structure effects on flow in porous media. PhD thesis, The University of Manchester, United Kingdom
- Bernaix J (1974) General report on theme 1. In: Proceedings of 3rd ISRM Conference, Vol. 1, Denver, United States
- Biao ZH, Tianyu YU, Wenfeng DI, Xianying LI (2017) Effects of pore structure and distribution on strength of porous Cu-Sn-Ti alumina composites. *Chin J Aeronaut* 30(6):2004–2015
- Brace WF (1981) The effect of size on mechanical properties of rock. *Geophys Res Lett* 8(7):651–652
- Cai M (2010) Practical estimates of tensile strength and Hoek-Brown strength parameter  $m_i$  of brittle rocks. *Rock Mech Rock Eng* 43(2):167–184
- Çelik SB (2017) The effect of cubic specimen size on uniaxial compressive strength of carbonate rocks from Western Turkey. *Arab J Geosci* 10(19):1–5
- Chang C, Zoback MD, Khaksar A (2006) Empirical relations between rock strength and physical properties in sedimentary rocks. *J Petrol Sci Eng* 51(3–4):223–237
- Cheng JL, Yang SQ, Chen K, Ma D, Li FY, Wang LM (2017) Uniaxial experimental study of the acoustic emission and deformation behavior of composite rock based on 3D digital image correlation (DIC). *Acta Mech Sin* 33(6):999–1021
- Cunha AP (1990) Scale effects in rock mass. In: Proceeding of International Workshop on Scale Effects in Rock Masses, Balkema
- Cvitanović NŠ, Nikolić M, Ibrahimbegović A (2015) Influence of specimen shape deviations on uniaxial compressive strength of limestone and similar rocks. *Int J Rock Mech Min Sci* 80:357–372
- Darlington WJ, Ranjith PG, Choi SK (2011) The effect of specimen size on strength and other properties in laboratory testing of rock and rock-like cementitious brittle materials. *Rock Mech Rock Eng* 44(5):513
- Dey TN, Wang CY (1981) Some mechanisms of microcrack growth and interaction in compressive rock failure. *Int J Rock Mech Mining Sci Geomech Abstracts* 18(3):199–209
- Diederichs MS (1999) Instability of hard rock masses: the role of tensile damage and relaxation. PhD thesis, University of Waterloo, Waterloo
- Diederichs MS (2003) Rock fracture and collapse under low confinement conditions. *Rock Mech Rock Eng* 36(5):339–381
- Diederichs MS (2007) The 2003 Canadian Geotechnical Colloquium: Mechanistic interpretation and practical application of damage and spalling prediction criteria for deep tunnelling. *Can Geotech J* 44(9):1082–1116
- Diederichs MS, Martin CD (2010) Measurement of spalling parameters from laboratory testing. In: Proceedings of the ISRM International Symposium-EUROCK 2010
- Du K, Su R, Tao M, Yang C, Momeni A, Wang S (2019) Specimen shape and cross-section effects on the mechanical properties of rocks under uniaxial compressive stress. *Bull Eng Geol Env* 78(8):6061–6074
- Dunham RJ (1962) Classification of carbonate rocks according to depositional texture. *Am Assoc Pet Geol Mem* 1:108–121



- Elliott GM, Brown ET (1985) Yield of a soft, high porosity rock. *Geotechnique* 35(4):413–423
- Esterhuizen E, Mark C, Murphy MM (2010) Numerical model calibration for simulating coal pillars, gob and overburden response. In: *Proceeding of the 29th international conference on ground control in mining*, Morgantown, WV, pp 46–57
- Fairhurst CE, Hudson JA (1999) Draft ISRM suggested method for the complete stress–strain curve for intact rock in uniaxial compression. *Int J Rock Mech Min Sci* 36:279–289
- Farahmand K, Vazaios I, Diederichs MS, Vlachopoulos N (2018) Investigating the scale-dependency of the geometrical and mechanical properties of a moderately jointed rock using a synthetic rock mass (SRM) approach. *Comput Geotech* 95:162–179
- Folk RL (1959) Practical petrographic classification of limestones. *AAPG Bull* 43(1):1–38
- Gao M, Liang Z, Li Y, Wu X, Zhang M (2018) End and shape effects of brittle rock under uniaxial compression. *Arab J Geosci* 11(20):614
- GOM (2016) Digital image correlation and strain computation basics. GOM, Braunschweig, Germany
- Hackston A, Rutter E (2016) The Mohr-Coulomb criterion for intact rock strength and friction—a re-evaluation and consideration of failure under polyaxial stresses. *Solid Earth* 7(2):493–508
- Hawkins AB (1998) Aspects of rock strength. *Bull Eng Geol Env* 57(1):17–30
- Hawkins A, McConnell BJ (1991) Influence of geology on geomechanical properties of sandstones. In: *Proceedings of the 7th ISRM Congress*
- Hemami B, Fakhimi A (2014) Numerical simulation of rock-loading machine interaction. In: *Proceedings of the 48th US Rock Mechanics/ Geomechanics Symposium*, Minneapolis, Minnesota Paper No. 74
- Hoek E, Brown ET (1980) *Underground excavations in rock*. Institute of Mining and Metallurgy, London
- Hoskins JR, Horino FG (1969) Influence of spherical head size and specimen diameters on the uniaxial compressive strength of rocks. US Department of the Interior, Bureau of Mines, Washington
- Jackson R, Lau JSO (1990) The effect of specimen size on the laboratory mechanical properties of Lac du Bonnet grey granite. In: *Proceedings of Scale effects in rock masses*, Balkema, Rotterdam
- Jaczkowski E, Ghazvinian E, Diederichs M (2017) Uniaxial compression and indirect tensile testing of Cobourg limestone: influence of scale, saturation and loading rate. Nuclear Waste Management Organization (NWMO-TR-2017-17)
- Jamshidi A, Nikudel MR, Khamehchiyan M, Sahamieh RZ (2016) The effect of specimen diameter size on uniaxial compressive strength, P-wave velocity and the correlation between them. *Geomech Geoeng* 11(1):13–19
- Kaiser PK, Kim B, Bewich RP, Valley B (2011) Rock mass strength at depth and implication for pillar design. *Min Technol* 120(3):170–179
- Kaklis KN, Maurigiannakis SP, Agioutantis ZG, Stathogianni FK, Steiakakis EK (2015) Experimental investigation of the size effect on the mechanical properties on two natural building stones. In: *Proceedings of 8th GRACM international congress on computational mechanics*, Greece
- Khishvand M, Akbarabadi M, Piri M (2016) Micro-scale experimental investigation of the effect of flow rate on trapping in sandstone and carbonate rock samples. *Adv Water Resour* 94:379–399
- Kong X, Liu Q, Lu H (2021) Effects of rock specimen size on mechanical properties in laboratory testing. *J Geotech Geoenviron Eng* 147(5):04021013
- Kranz RL (1983) Microcracks in rocks: a review. *Tectonophysics* 100(1–3):449–480
- Lan H, Martin CD, Hu B (2010) Effect of heterogeneity of brittle rock on micromechanical extensile behavior during compression loading. *J Geophys Res Solid Earth*. <https://doi.org/10.1029/2009JB006496>
- Li D, Song S, Zuo D, Wu W (2020) Effect of pore defects on mechanical properties of graphene reinforced aluminum nanocomposites. *Metals* 10(4):468
- Li H, Song K, Tang M, Qin M, Liu Z, Qu M, Li B, Li Y (2021) Determination of scale effects on mechanical properties of Berea Sandstone. *Geofluids* 2021:1–12
- Liaw HK, Kulkarni R, Chen S, Watson AT (1996) Characterization of fluid distributions in porous media by NMR techniques. *AIChE J* 42(2):538–546
- Marker BR (2015) Bath stone and purbeck stone: a comparison in terms of criteria for global heritage stone resource designation. *Episodes* 38(2):118–123
- Martin CD, Chandler NA (1994) The progressive fracture of Lac du Bonnet granite. *Int J Rock Mech Mining Sci Geomech Abstracts* 31(6):643–659
- Martin CD (1997) Seventeenth Canadian geotechnical colloquium: the effect of cohesion loss and stress path on brittle rock strength. *Can Geotech J* 34(5):698–725
- Masoumi H (2013) Investigation into the mechanical behaviour of intact rock at different sizes. Doctor of Philosophy thesis, University of New South Wales, Sydney
- Masoumi H, Saydam S, Hagan PC (2016) Unified size-effect law for intact rock. *Int J Geomech* 16(2):04015059
- Malyszko L, Bilko P, Kowalska E (2017) Determination of elastic constants in Brazilian tests Using Digital Image Correlation. In: *Proceedings of the 2017 Baltic Geodetic Congress (BGC Geomatics)*, pp 153–157
- Mogi K (1961) The influence of the dimensions of specimens on the fracture strength of rocks. *Bull Earthquake Res Inst* 40:175–185
- Mokhtari M, Nath F, Hayatdavoudi A, Nizamutdinov R, Jiang S, Rizvi H (2019) Complex deformation of naturally fractured rocks. *J Petrol Sci Eng* 183:106410
- Mortazavi A, Hassani FP, Shabani M (2009) A numerical investigation of rock pillar failure mechanism in underground openings. *Comput Geotech* 36(5):691–697
- Munoz H, Taheri A, Chanda EK (2016) Pre-peak and post-peak rock strain characteristics during uniaxial compression by 3D digital image correlation. *Rock Mech Rock Eng* 49(7):2541–2554
- Nishimatsu Y, Yamaguchi U, Motosugi K, Morita M (1969) The size effect and experimental error of the strength of rocks. *J Min Mater Process Inst Jpn* 18:1019–1025
- Niu Y, Wang H, Shao S, Park SB (2016) In-situ warpage characterization of BGA packages with solder balls attached during reflow with 3D digital image correlation (DIC). In: *Proceedings of the 2016 IEEE 66th Electronic Components and Technology Conference*, pp 782–788
- Nomikos P, Kaklis K, Agioutantis Z, Mavrigiannakis S (2020) Investigation of the size effect and the fracture process on the uniaxial compressive strength of the banded Alfas porous stone. *Procedia Struct Integrity* 26:285–292
- Pan B, Qian K, Xie H, Asundi A (2009) Two-dimensional digital image correlation for in-plane displacement and strain measurement: a review. *Meas Sci Technol* 20(6):062001
- Pells PJ (2004) On the absence of size effects for substance strength of Hawkesbury Sandstone. *Australian Geomech* 39(1):79–83
- Perras MA, Diederichs MS (2014) A review of the tensile strength of rock: concepts and testing. *Geotech Geol Eng* 32(2):525–546
- Pratt HR, Black AD, Brown WS, Brace WF (1972) The effect of specimen size on the mechanical properties of unjointed diorite. *Int J Rock Mech Mining Sci Geomech Abstracts* 9(4):513–516
- Prat M, Bisch P, Millard A, Mestat P, Pijaudier-Calot G (1995) *La modélisation des ouvrages*, vol 4. Hermes, Paris

- Quiñones J, Arzúa J, Alejano LR, García-Bastante F, Ivars DM, Walton G (2017) Analysis of size effects on the geomechanical parameters of intact granite samples under unconfined conditions. *Acta Geotech* 12(6):1229–1242
- Renani HR, Martin CD (2018) Modeling the progressive failure of hard rock pillars. *Tunn Undergr Space Technol* 74:71–81
- Schwartz E, Saralaya R, Cuadra J, Hazeli K, Vanniamparambil PA, Carmi R, Kontsos A (2013) The use of digital image correlation for non-destructive and multi-scale damage quantification. In: *Proceedings of the Sensors and Smart Structures Technologies for Civil, Mechanical, and Aerospace Systems 2013*, International Society for Optics and Photonics 86922H
- Shirole D, Walton G, Hedayat A (2020) Experimental investigation of multi-scale strain-field heterogeneity in rocks. *Int J Rock Mech Min Sci* 127:104212
- Sinha S, Walton G (2018) A progressive S-shaped yield criterion and its application to rock pillar behavior. *Int J Rock Mech Min Sci* 105:98–109
- Sinha S, Walton G (2021) Investigation of pillar damage mechanisms and rock-support interaction using Bonded Block Models. *Int J Rock Mech Min Sci* 138:104652
- Sinha S, Shirole D, Walton G (2021) Investigation of the micromechanical damage process in a granitic rock using an inelastic bonded block model (BBM). *J Geophys Res: Solid Earth* 125(3):55
- Sitepu H (2009) Texture and structural refinement using neutron diffraction data from molybdenite (MoO<sub>3</sub>) and calcite (CaCO<sub>3</sub>) powders and a Ni-rich Ni<sub>50</sub>. 7Ti<sub>49</sub>. 30 alloy. *Powder Diffr* 24(4):315–326
- Sjöberg T, Kajberg J, Oldenburg M (2017) Fracture behaviour of Alloy 718 at high strain rates, elevated temperatures, and various stress triaxialities. *Eng Fract Mech* 178:231–242
- Sprunt ES, Brace WF (1974) Direct observation of microcavities in crystalline rocks. *Int J Rock Mech Mining Sci Geomech Abstracts* 11(4):139–150
- Stróżyk J, Tankiewicz M (2016) The elastic undrained modulus  $E_{u50}$  for stiff consolidated clays related to the concept of stress history-ryad normalized soil properties. *Studia Geotechnica Et Mechanica* 38(3):67–72
- Sutton MA, Orteu JJ, Schreier H (2009) *Image correlation for shape, motion and deformation measurements: basic concepts, theory and applications*. Springer Science & Business Media, USA
- Tang Y, Okubo S, Xu J, Peng S (2019) Experimental study on damage behavior of rock in compression–tension cycle test using 3D Digital Image Correlation. *Rock Mech Rock Eng* 52(5):1387–1394
- Tang CA, Tham LG, Lee PK, Tsui Y, Liu H (2000) Numerical studies of the influence of microstructure on rock failure in uniaxial compression—part II: constraint, slenderness and size effect. *Int J Rock Mech Min Sci* 37(4):571–583
- Tapponnier P, Brace WF (1976) Development of stress-induced microcracks in Westerly granite. *Int J Rock Mech Mining Sci Geomech Abstracts* 13(4):103–112
- Thuro K, Plinninger RJ, Zäh S, Schütz S (2001) Scale effects in rock strength properties. Part I: Unconfined compressive test and Brazilian test. In: *Proceedings of ISRM regional symposium*, pp 169–174
- Trilion Quality Systems (2020) *Aramis training: surface preparation and patterning*
- Trilion Quality Systems (2021) *How accurate are my measurements?* <https://faq.trilion.com/docs/how-accurate-are-my-measurements>. Accessed 6 Dec 2021
- Tuncay E, Hasancebi N (2009) The effect of length to diameter ratio of test specimens on the uniaxial compressive strength of rock. *Bull Eng Geol Env* 68(4):491–497
- Vutukuri VS, Lama RD, Saluja SS (1974) *Handbook on mechanical properties of rocks*. Trans Tech Publications, Bay Village, OH
- Walton G, Hedayat A, Kim E, Labrie D (2017) Post-yield strength and dilatancy evolution across the brittle–ductile transition in Indiana limestone. *Rock Mech Rock Eng* 50(7):1691–1710
- Walton G (2018) Scale effects observed in compression testing of Stanstead granite including post-peak strength and dilatancy. *Geotech Geol Eng* 36(2):1091–1111
- Walton G, Arzúa J, Alejano LR, Diederichs MS (2015) A laboratory-testing-based study on the strength, deformability, and dilatancy of carbonate rocks at low confinement. *Rock Mech Rock Eng* 48(3):941–958
- Walton G (2021) A new perspective on the brittle–ductile transition of rocks. *Rock Mech Rock Eng* 10:1–4
- Weber J, Cheshire MC, Bleuel M, Mildner D, Chang YJ, Ievlev A, Littrell KC, Ilavsky J, Stack AG, Anovitz LM (2021) Influence of microstructure on replacement and porosity generation during experimental dolomitization of limestones. *Geochim Cosmochim Acta* 303:137–158
- Weibull W (1939) *A statistical theory of strength of materials*. IVB-Handl.
- Wong TF, Baud P (2012) The brittle–ductile transition in porous rock: a review. *J Struct Geol* 44:25–53
- Xing HZ, Zhang QB, Ruan D, Dehkhoda S, Lu GX, Zhao J (2018) Full-field measurement and fracture characterisations of rocks under dynamic loads using high-speed three-dimensional digital image correlation. *Int J Impact Eng* 113:61–72
- Yoshinaka R, Osada M, Park H, Sasaki T, Sasaki K (2008) Practical determination of mechanical design parameters of intact rock considering scale effect. *Eng Geol* 96(3–4):173–186
- Zhai H, Masoumi H, Zoorabadi M, Canbulat I (2020) Size-dependent behaviour of weak intact rocks. *Rock Mech Rock Eng* 53(8):3563–3587

**Publisher's Note** Springer Nature remains neutral with regard to jurisdictional claims in published maps and institutional affiliations.

Springer Nature or its licensor (e.g. a society or other partner) holds exclusive rights to this article under a publishing agreement with the author(s) or other rightsholder(s); author self-archiving of the accepted manuscript version of this article is solely governed by the terms of such publishing agreement and applicable law.